

# Flutter Tests of the Pazy Wing

Ariel Drachinsky\*, Or Avin<sup>†</sup>, Daniella E. Raveh<sup>‡</sup>  
Technion - Israel Institute of Technology, Haifa, Israel

Yaron Ben-Shmuel<sup>§</sup>  
Rafael, Advanced Defense Systems, Israel

Moshe Tur<sup>¶</sup>  
Tel-Aviv University, Ramat-Aviv, Israel

**The paper presents the flutter and LCO tests of the Pazy wing, a very flexible wing model designed to study aeroelastic phenomena associated with nonlinear geometry and provide data for nonlinear aeroelastic model validation. The Pazy wing model, analyses, and data from earlier aeroelastic tests are provided in Ref. [1]. In the current study, three velocity sweeps were performed at different angles of attack (AoA), during which the wing entered and exited limit-cycle oscillations (LCO). A motion recovery camera system and fiber-optics Bragg grating sensors were used to track the deformations and strains over the wingspan. The wing encountered LCO when the wingtip deformation was approximately 25% of the span. The onset velocity, frequency, and mode shape varied depending on the test's AoA. The paper first focuses on the onset of the oscillations, where the onset velocity and oscillation mode-shapes are analyzed. The paper then continues to investigate the LCO characteristics and the nonlinear behavior of the wing. The wing models and experimental data are publicly available through the 3rd Aeroelastic Prediction Workshop (<https://nescacademy.nasa.gov/workshops/AePW3/public>).**

## I. Introduction

The Pazy wing is an aeroelastic benchmark of a very flexible wing. The 100 mm chord 550 mm span straight wing model was designed to display very large deformations, in the order of half the span, and low strains under aerodynamic loading. The wing was tested at the subsonic wind tunnel at the Faculty of Aerospace Engineering, Technion, in various flow conditions. Structural data collected include displacements over the wingspan, measured by a motion recovery camera system (MRS), and strain data, measured by Bragg Grating fiber-optic sensors (FOS). Avin et al. [1] presented the wing design, analyses, and results of two wind-tunnel tests - A test in which the wing was mounted on a force balance, and a test in which the wing was mounted directly to the wind-tunnel floor. Both tests included angle of attack

---

\*Research Associate, Rafael, Advanced Defense Systems, AIAA Member

<sup>†</sup>Graduate Student, Faculty of Aerospace Engineering, Technion, AIAA Student Member

<sup>‡</sup>Professor, Faculty of Aerospace Engineering, Technion, AIAA Associate Fellow

<sup>§</sup>Senior Research Associate, Rafael, Advanced Defense Systems

<sup>¶</sup>Professor, School of Electrical Engineering, Tel-Aviv University

(AoA) sweeps at fixed airspeeds, and velocity sweeps at fixed root AOA values. At the -5, 5, and 7 degrees AoA velocity sweeps, the wing became unstable and exhibited limit cycle oscillations (LCO) at dynamic pressure values in which the wingtip was deflected to approximately 25% of the span. A third wind-tunnel test, described in the current study, focuses on flow conditions at which the wing is unstable.

Flutter analyses were performed using two computational tools, [2] the Modal Rotation Method (MRM) [3] and Sharpy, [4], both accounting for structural nonlinearity due to large deformations. The computational study of Refs. [3] and [2] guided the current experimental campaign, and their computational results are briefly repeated here. The paper presents the Pazy wing design, its structural dynamic properties, linear and nonlinear flutter analyses, and results from the flutter tests. The conditions selected for the flutter tests aimed to establish the stability and instability regions of the Pazy wing and compare them to those from the computational analysis.

## II. Wing Design

The Pazy wing model was designed to experience very large deformations, in the order of 50% span under static aerodynamic loading. It was designed for testing in the subsonic wind-tunnel of the Faculty of Aerospace Engineering, Technion, which has a test chamber of 1 by 1 m and operates in airspeeds of 10-100 m/s.

The Pazy wing has a chord length of 100 mm a span of 550 mm, and a NACA0018 airfoil. The wing structure is made of an Aluminum 7075 spar, of dimensions 550 mm (length) by 60 mm (width) by 2.25 mm (thickness), and a Nylon 12, 3D printed chassis. The wing is covered with Oralight Polyester film using an iron to activate the thermo-active adhesive. The wing design is such that the main stiffness-contributor (both in torsion and bending) is the aluminum plate, which provides about 85% of the stiffness. The aluminum plate is thin and thus experiences small strains.

A 300 mm long and 10 mm diameter wing-tip rod and a 120 mm diameter and 22 mm thick base are 3D printed as part of the chassis. The wing-tip rod is used for attaching weights (via drilled holes) that can modify the dynamic properties of the structure and alter the flutter characteristics. The base is used as an interface to connect the wing to the wind tunnel floor. Based on the CAD model and nominal material properties, the wing, without the base, weighs 328 gr. Based on weighing, the wing weight with the accelerometer, wiring, and adhesives the wing's actual weight is estimated as 361 gr (without the segment of the main spar that protrudes the base). Tabel 1 provides the nominal material properties. Details on the wing assembly and stress analyses are provided in Ref. [1].

**Table 1 Nominal Material Properties**

Material	Density	Young's Modulus (MPa)	Poisson's Ratio	Yield Strength (MPa)	Ultimate Tensile Strain
Aluminum 7075-T6	2795 ( $kg/m^3$ )	71000	0.33	468	8%
Aluminum 6061-T651	2712 ( $kg/m^3$ )	71000	0.33	245	10%
Nylon 12	930 ( $kg/m^3$ )	1700	0.394	48	25%
Oralight*	36 ( $g/m^2$ )	4666	0.4	80	25%

\* Material properties derived from tensile test, see [1]

### III. Aeroelastic Analyses

Figure 1 shows the Nastran FE model that was used to compute the dynamic properties of the wing. The aluminum spar is modeled with plate elements and the Nylon parts are modeled using plate and beam elements. The Polyester skin, not shown in Fig 1, is modeled with plate elements. It's contribution to the wing stiffness and frequencies is small [1]. Details on the FE model adaptation based on static loading tests and ground vibration tests are provided in Ref. [1].

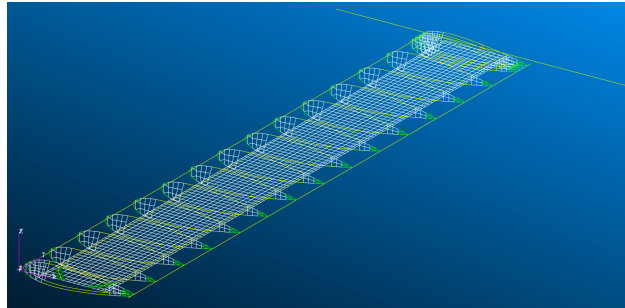


**Fig. 1 Finite-element model**

**Free-vibration Analysis** Linear free-vibration analysis provided the structure's natural frequencies and mode shapes, which were then used for flutter analysis and as the basis for the nonlinear aeroelastic analysis using the MRM [2, 3]. Figure 2 shows the first four low-frequency modes of the wing and their corresponding frequencies.

#### A. Linear Flutter Analysis

Linear flutter analysis was performed using the ZAERO aeroelastic analysis software based on a linear panel aerodynamic model [5]. Figure 3 shows the  $\omega - V - g$  plot, presenting the variation of the frequencies and damping as a function of airspeed. Flutter onset was computed at  $67m/s$  and a frequency of  $34.5Hz$ . The flutter mode is a hump mode combination of first torsion and second bending. Divergence instability appears at  $83m/s$  and an additional flutter instability, involving the first bending and first torsion modes is computed at  $96m/s$  and a frequency of  $16.7Hz$ . Flutter

analysis was based on the first 10 low-frequency modes. Only the first six are shown in Fig 3. The in-plane bending mode, at 106 Hz in the FE model, does not contribute to the linear aeroelastic interaction.

## B. Nonlinear Flutter Analysis

Nonlinear flutter analyses were computed with the MRM [3]. The MRM is a modal-based methodology that is intended for complex structures, for which the generation of an equivalent beam model is impossible or requires considerable effort. In the MRM, the structural formulation is based on curvature mode shapes that are computed in a finite-element free-vibration analysis [6]. For aeroelastic analyses, the MRM method is coupled with an aerodynamic model to compute nonlinear static aeroelastic responses and dynamic stability. [3] While the MRM is not limited to analyzing beams, it solves the structural deformations along a reference line. For wing structures, this line runs over the wing-span, typically along the mid-chord, the leading or trailing-edge. The modes are described in segments over the reference line. The dynamic and unsteady aerodynamic models of the deformed wing are evaluated by manipulation of the models of the undeformed shape, as detailed in Ref. [3].

Figure shows an  $\omega - V - g$  plot of a matched flutter analysis in which each frequency and damping point is computed in a linearized solution about the deformed shape at the corresponding velocity and AoA, at three typical AoA values. The flutter mode couples the wing's first torsion and second-bending modes, and occurs as the frequency of the torsion mode reduces with airspeed, to meet the second-bending frequency. Figure 4(a) shows that this flutter mode is a hump mode, regaining stability at higher airspeeds, as the torsion frequency reduces below that of the second-bending mode (as seen in 4(b)). As the AoA is increased, flutter onset occurs at a lower airspeed due to the larger drop in the torsion mode frequency, and the hump mode becomes narrower. This is also seen in Fig 5, taken from Ref. [3], that shows the computed flutter boundaries and stable (white) and unstable (pink) regions, in terms of airspeed and AoA.

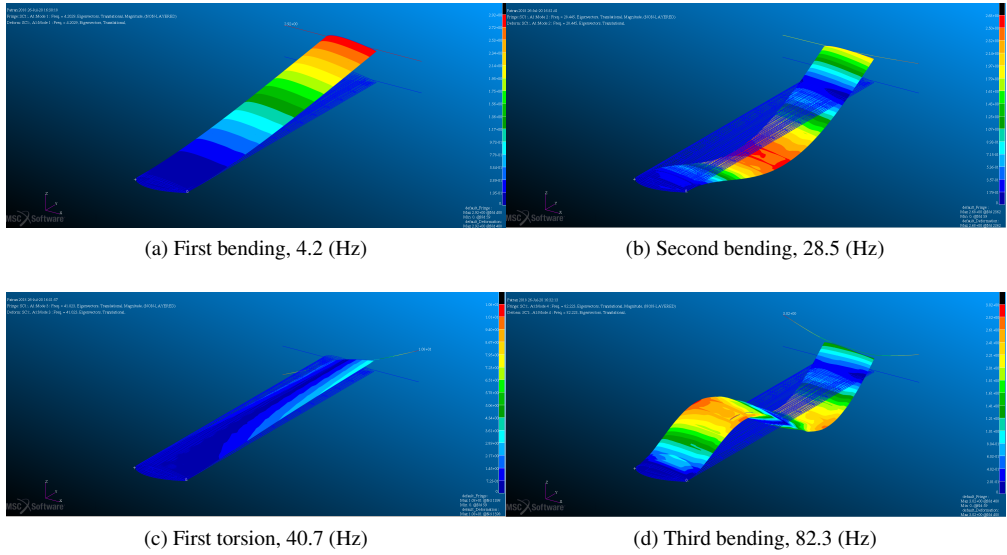


**Fig. 2 First four mode shapes and frequencies of the Pazy wing with skin**

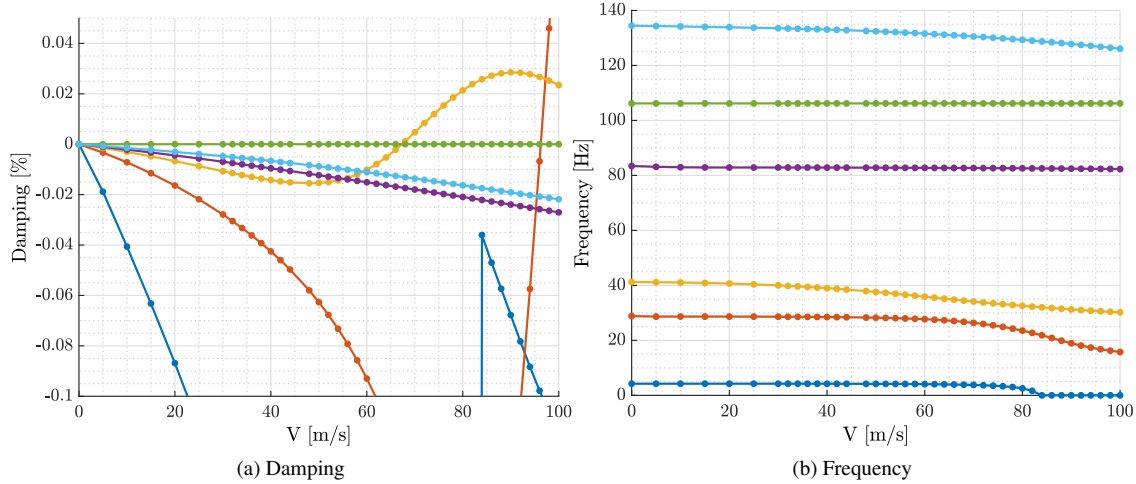


**Fig. 3  $\omega - V - g$  plot, presenting the variation of the frequencies and damping as a function of airspeed**

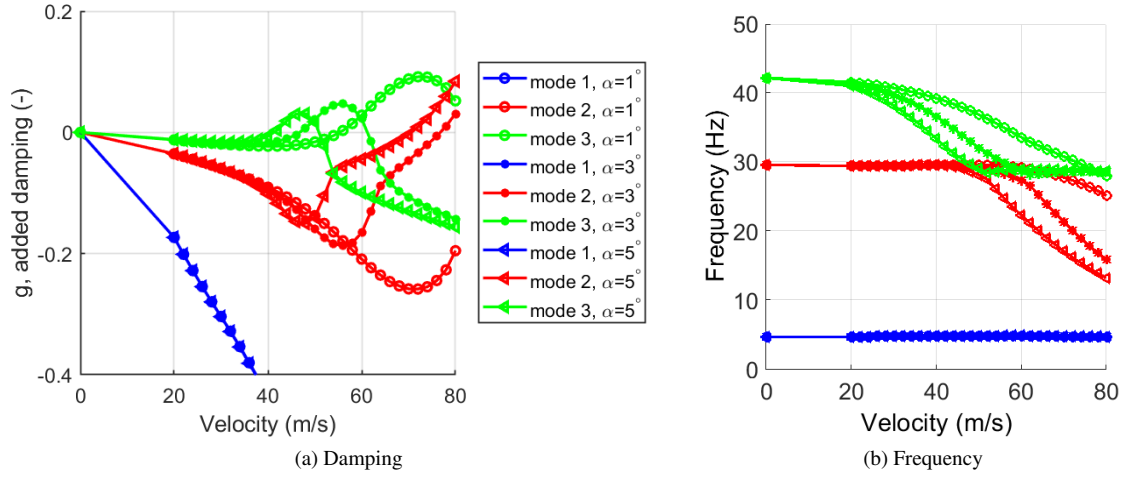


**Fig. 4** Matched  $V - g$  (left) and  $V - \omega$  (right) plots at three AoAs

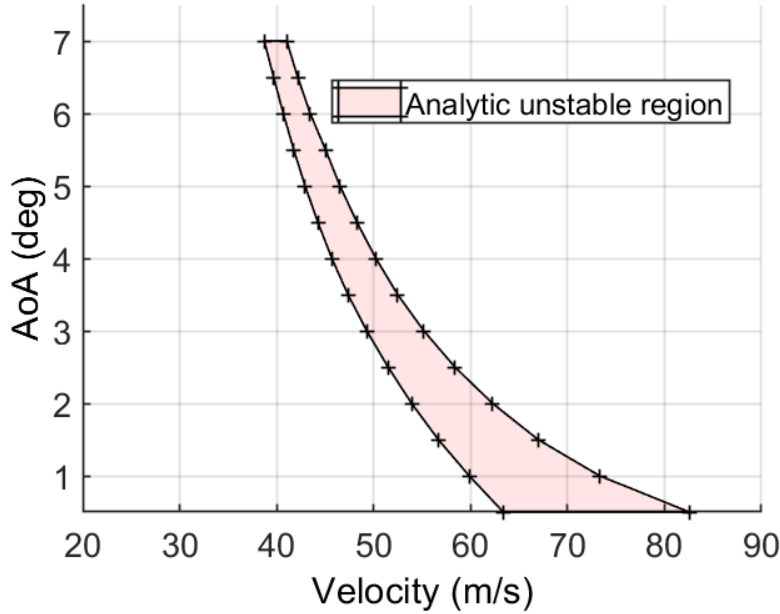


**Fig. 5** Flutter boundaries and unstable region

#### IV. Wind Tunnel Tests

##### A. Structural Measurements (Instrumentation)

Wing deformations were captured by an OptiTrack\* motion recovery system (MRS) that tracks infra-red markers taped onto the wing. The system measures translations in X, Y, and Z directions, defined during the initial calibration procedure (X in the chord direction, Y in the wing span direction, and Z is the out-of-plane direction). 24 infra-red reflector stickers were attached to the wing, over the leading- and trailing-edges, and the center chord (Fig 6(a)).

\*<http://optitrack.com>

Additional three reflectors were attached to the wingtip bar.

The wing was instrumented with strain-measuring optical fibers. Four optical fibers with inscribed Bragg gratings were affixed to one surface of the aluminum spar, providing strain measurement at 30 points over each of the leading- and trailing edges of the spar. The four fibers were set into two 1 mm wide and 0.1 mm deep cavities along the aluminum spar span length, located at 22 mm from the leading edge and 21.3 mm from the trailing edge. Figure 6(b) shows the FBG sensor locations marked in red and blue (on the two fibers).

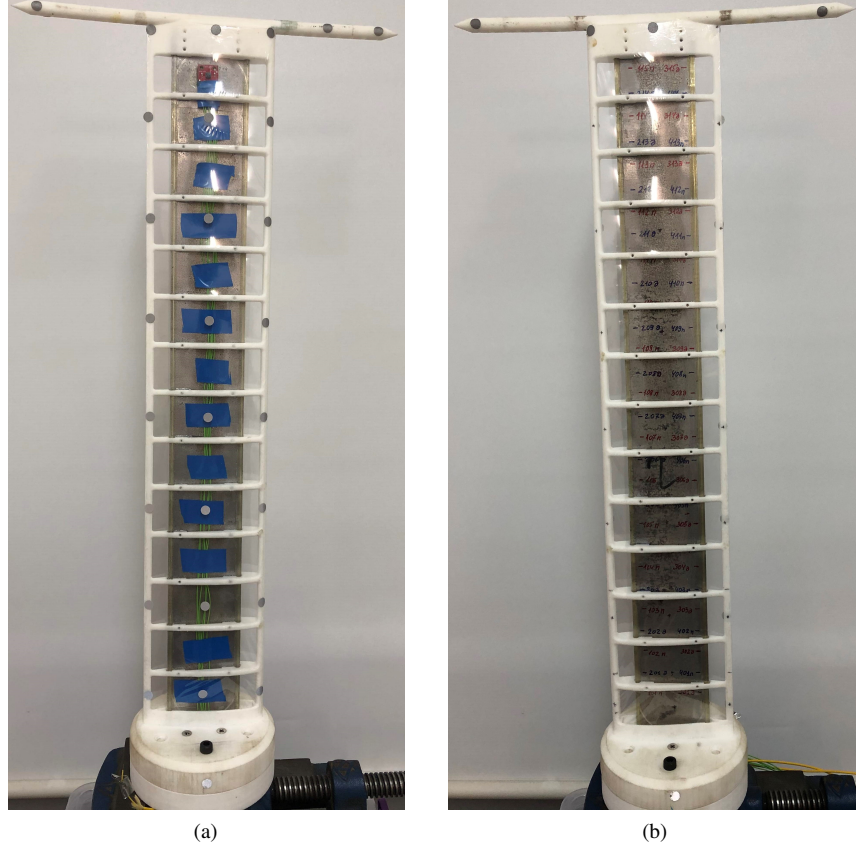


**Fig. 6 Instrumented Wing - MRS IR reflectors (a) and FBG strain sensors (b)**

## B. Flutter test description and general trends

Three velocity sweeps, at a fixed AoA value, were conducted as follows:

- 1) At a root AoA of 7 degrees, the airspeed was increased from zero to approximately 50 m/s to get into and out of the instability region. The AoA was then decreased to 5 degrees while keeping the airspeed fixed. The airspeed was decreased to zero, again passing through the unstable region. The wind-tunnel airspeed and AoA variation during the test are shown in Figure 7(a).
- 2) This exercise was repeated increasing the airspeed at fixed 5 degrees AoA and decreasing it at 3 degrees. The

wind-tunnel airspeed and AoA variation during the test are shown in Figure 7(b).

- 3) This exercise was repeated increasing the airspeed at fixed 3 degrees AoA and decreasing it at 1 degree. The wind-tunnel airspeed and AoA variation during the test are shown in Figure 7(c).

We note that in several cases, there were slight differences between the commanded and actual AoA values. These are evident in small changes in the AoA (about 0.1 degree) at the onsets and in the overshoots at the AoA reduction.

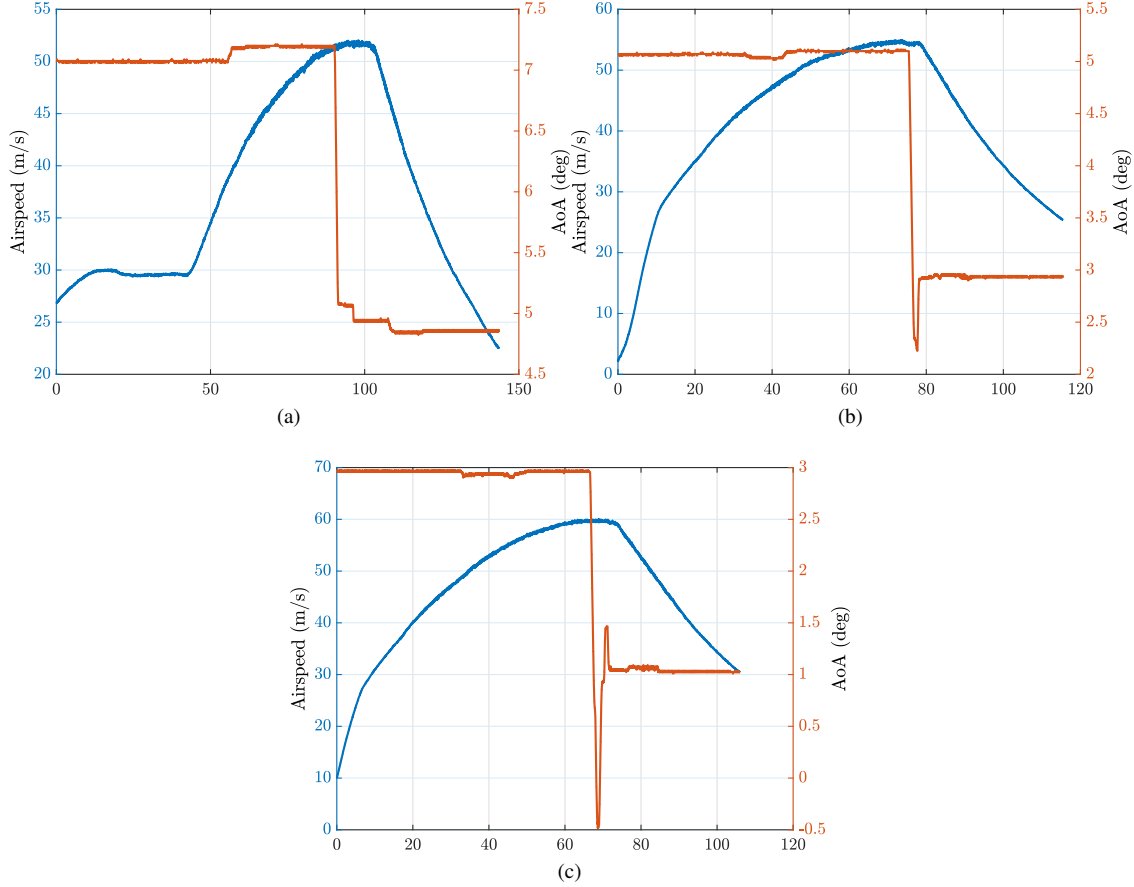


**Fig. 7** Airspeed and AoA variations at the flutter tests

Due to the erratic large oscillations of the wing during LCO, some of the MRS and FOS measurements were damaged. The MRS system experienced tracking errors likely due to reflections from the wing's skin, large deformation gradients (with respect to the exposure time), and line of sight losses. At low velocities and small deformations, these tracking errors are relatively small. The damage in the FOS data is likely due to the large values of oscillatory strains. These could have caused large shifts in the Bragg sensor frequencies, which may have overlapped frequencies of adjacent sensors.

Figure 8 shows a sample data from a single strain sensor, located 127 mm from the root on the main spar, as a function of time, together with the airspeed variation. This test starts at AoA of seven degrees, which is reduced to five

degrees at approximately 85 seconds. The strain values in Fig. 8 are multiplied by  $-1$  to make them easier to read with the airspeed data. The quasi-steady variation of the strain corresponds to the increase in the dynamic pressure (airspeed increase) with time. The strong strain oscillations correspond to periods of LCO wing motion. The sharp reduction in the strain value at about 85 seconds corresponds to the AoA reduction from seven to five degrees. We note that the oscillation amplitudes at five degrees AoA (second LCO) are larger than at seven degrees (first LCO).

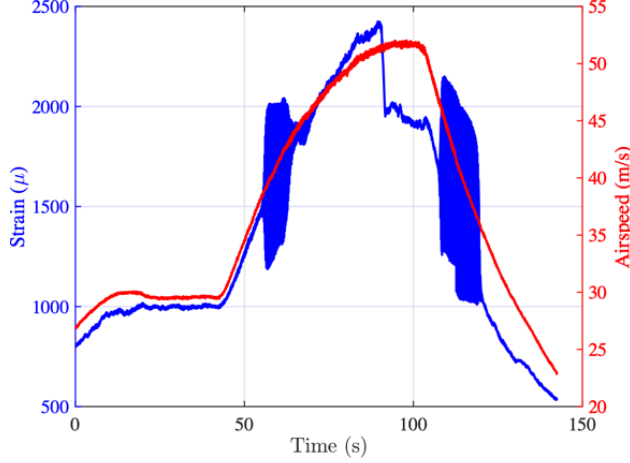


**Fig. 8 Strain at a single sensor and airspeed variation at a flutter test**

Figure 9 shows the strains versus the velocity obtained at five degrees, once while increasing the airspeed and once while decreasing it. Hysteresis is observed in the LCO onset and offset conditions. This indicates a supercritical bifurcation in which multiple solutions can be obtained at a certain velocity depending on the initial conditions. Given a sufficiently large perturbation, the wing might oscillate at velocities at which, based on the linearized solution, it is stable.

### C. Flutter characteristics

Figures 10, 11, and 12, show the available wingtip displacement and twist angle time histories obtained from the MRS and reconstructed from the strains using linear and nonlinear strain to displacement (STD) transformation methods [7]. Figure 10(a) shows the flutter onset is marked in a rectangle and the insert plot shows a comparison of the deflections as obtained with different methods right before the LCO start. There is a good agreement between the dynamic wingtip deflections measured and computed by the different methods, and the flutter onset is evident. For the wingtip twist, in Fig. 10(b), only the linear STD reconstruction is presented. The twist angles obtained with the nonlinear method are almost identical. The MRS data was too erratic to estimate the wingtip twist angle adequately. This can be seen from Fig. 11(a), showing a displacement tracking error. In terms of displacement, this is a small error. However, it translates to several degrees in the twist. During the oscillating motion, and after it, these errors grow even further, which is the reason that for further analyses, we use mostly the strain-based data, while the MRS mainly serves for calibration and a

sanity check during the first stages of each test.

The third test, at three and one degrees AoA, somewhat differs from the other two tests. In this test, flutter was encountered while the angle of attack was reduced from three to one degrees, at fixed airspeed (and not in a fixed AoA during a velocity sweep as in the other two tests). The AoA at which the flutter started was assessed based on the wingtip displacements and AoA shown in the insert in Fig. 12(a). It is not an accurate estimate, as the AoA decrease was rapid (over about one second) thus not enabling an exact identification of the AoA at which the oscillations started.

Both the wingtip displacement and twist angle time histories indicate the airspeeds at which the wing became unstable and re-stabilized while increasing or decreasing the airspeed. These airspeeds are summarized in table 2 and compared to the analytic prediction. The arrows next to the AoA values indicate whether the test was of increasing or decreasing airspeed. Figure 13 shows the flutter velocities obtained in the test, plotted on top of the MRM stability map. The red triangles indicate flutter onset velocities and the green ones indicate flutter offset velocities. The direction of the triangles indicates the direction of the airspeed change. The legend indicates if the onset/offset was at increasing airspeed ('Test onset up') or decreasing airspeed ('Test onset down'). Table 2 and Fig. 13 indicates a good agreement between the computed and test onset speeds. The analysis cannot predict the offset speed as it is based on linearization about a steady condition, which is not the case for the offset.

**Table 2 Flutter onset/offset airspeeds**

AoA (°)	analytic flutter onset velocity (m/s)	test flutter onset velocity (m/s)	error (%)	test flutter offset velocity	flutter onset deflection (% span)
7 ↑	38.7	38	1.8	46	26
5 ↓	46.5	48	3.1	36	31.5
5 ↑	42.9	43	0.2	51	24.5
3 ↓	55.2	55	0.4	40	28.5
3 ↑	49.2	49	0.4	58	23
2 – 2.5 ↓	62.2-58.4	60	0-3.7	44	29

Another interesting aspect to examine is the frequency and mode shape at the start of the oscillations, when the nonlinearity of the response is relatively weak. This can be approximately considered as the flutter frequency and mode shape. Figure 14 shows the oscillatory wingtip displacement and twist angle close to flutter onset at 5 degrees AoA, during up and down velocity sweeps. The response data was high-pass filtered at 15Hz to capture only the oscillatory part and filter out the quasi-steady and the first mode responses. From these plots, the ratio between the wingtip deflection and twist angle can be derived, as well as the phase angle between them. These are summarized in Table 3. On the up-sweep, the wingtip twist lags the displacement by  $113^\circ$ , while on the down sweep the lag is  $132^\circ$ <sup>†</sup>. We note that this phase is the opposite of a typical first-bending first-torsion flutter mechanism, in which the twist angle is in phase with the displacement velocity, leading the displacement itself. This is because in the current mechanism, which

<sup>†</sup>A Positive phase is defined when the twist lags the displacement

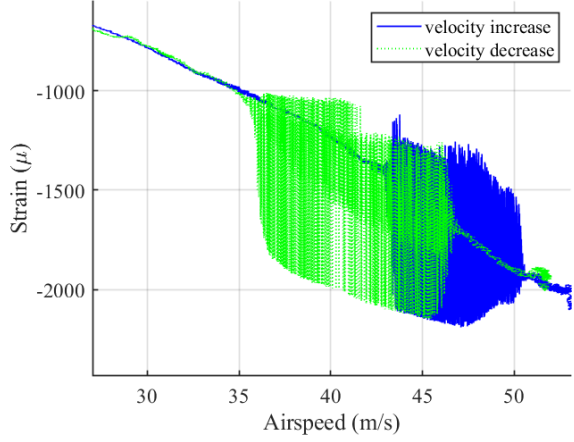


**Fig. 9** Strain versus airspeed at LCO at AoA of five degrees; LCO entered while increasing/decreasing the airspeed

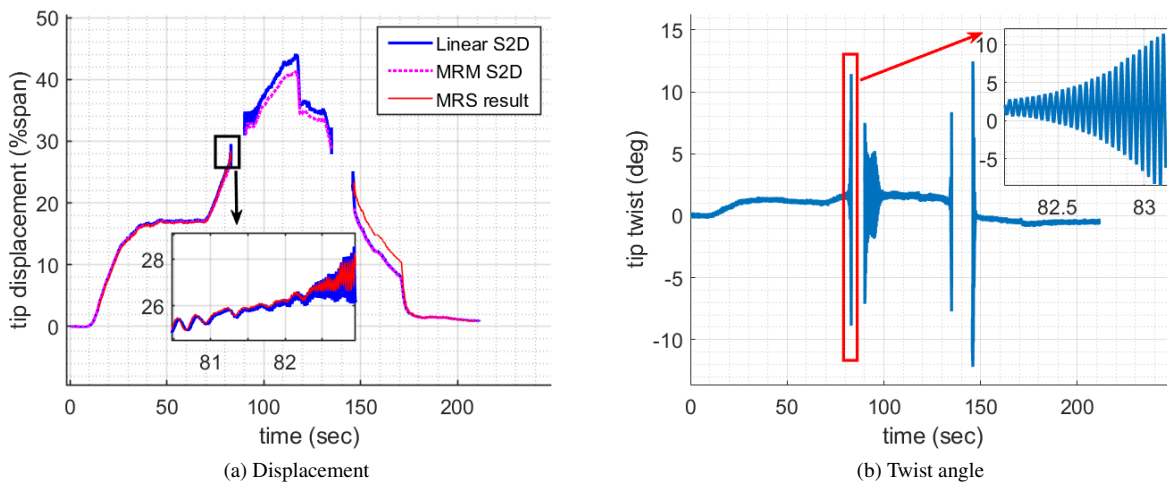


**Fig. 10** Wingtip displacement and twist angle at the first flutter test (AoA of 7 and 5 degrees)

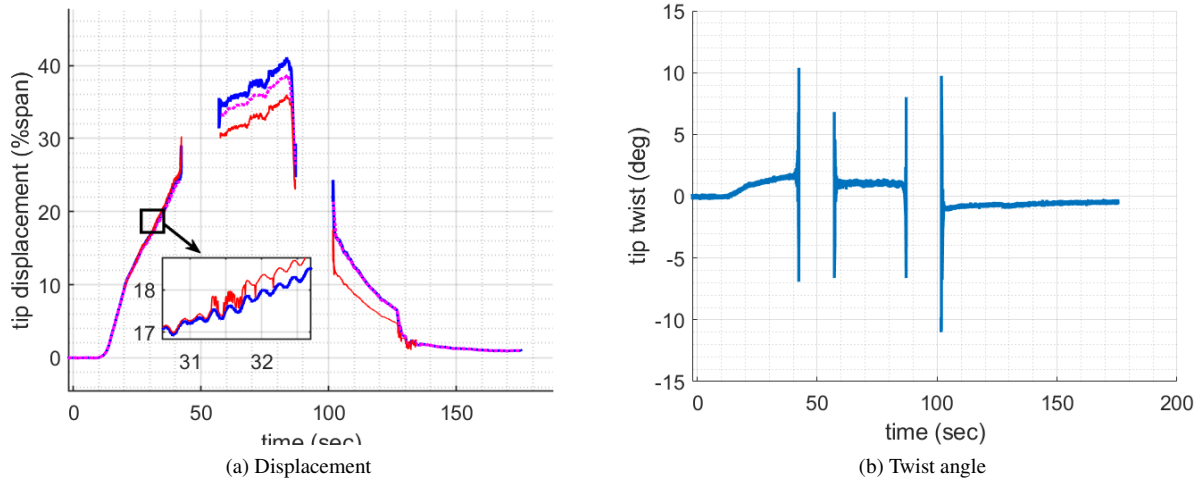


**Fig. 11** Wingtip displacement and twist angle at the second flutter test (AoA of 5 and 3 degrees)

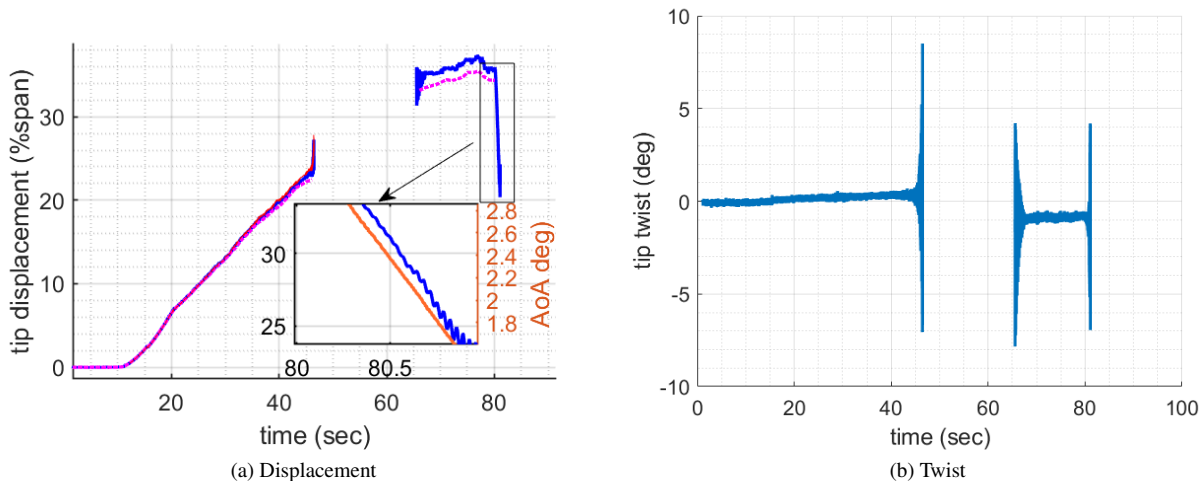


**Fig. 12** Wingtip displacement and twist angle at the third flutter test (AoA of 3 and 1 degrees)

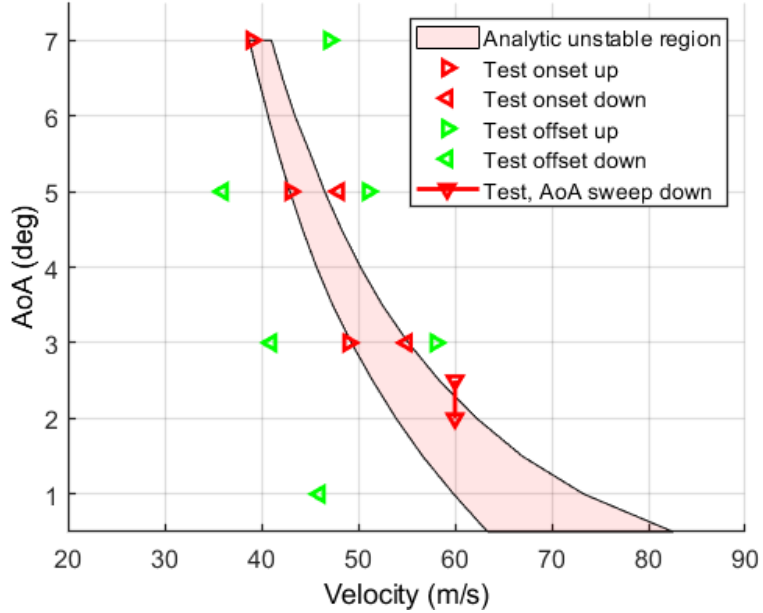


**Fig. 13 Comparison of computational and experimental flutter onset/offset airspeeds**

involves the second bending motion, the displacement over most of the wing is out of phase with the wingtip. hence, the phase between the modes (modal phase) can be defined by abstracting  $180^\circ$  from the phase between the tip displacement and twist. Based on data from several points on the wing, the accuracy of the data in Table 3 is  $0.25(\text{ }^\circ/\%\text{span})$  and  $5^\circ$  in the amplitude ratio and phase angle respectively.

From Table 3, it is seen that the amplitude ratio and phase angle is different during the onset and offset phases. Also, the phase angles between the modes are significantly smaller at the higher flutter velocities, obtained during the down-sweeps, than those at the lower velocities, obtained during the up-sweeps. The ratio between the wingtip displacement and twist is also smaller at the higher velocities. Small deviations are also seen between flutter modes at different AoAs. The flutter frequency slightly increases with the AoA (and deformation, see Table 13), as does the twist to displacement ratio, while in the phase angle, no clear trend can be observed.

Examination of the displacements and twist angles in figures 10,11, and 12 hints that the main source of nonlinearity in the system, which governs the LCO, is aerodynamic. While the tip deflection dynamic amplitude in the measured region is only a few percent of the span, the wingtip twist angles oscillate at an amplitude of  $\approx 10^\circ$ , at which the airfoil is expected to stall. This is also seen in table 3 by the large ratio between the twist angle and the displacement.

#### D. LCO Characteristics

The measured strain data from an arbitrary strain sensor was analyzed in the frequency domain. Figure 15 shows Spectrogram plots of the data, at the three test AoAs, presenting the variation of the frequency content of the signal with

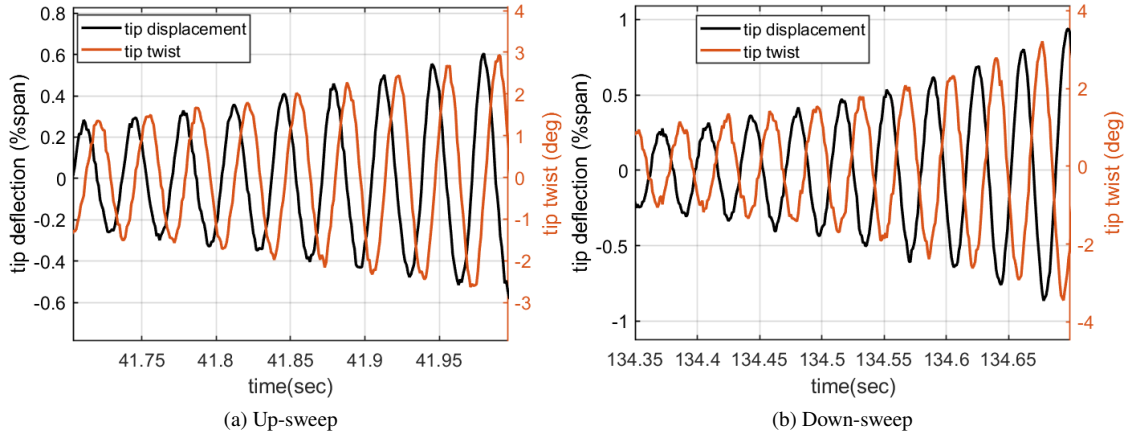
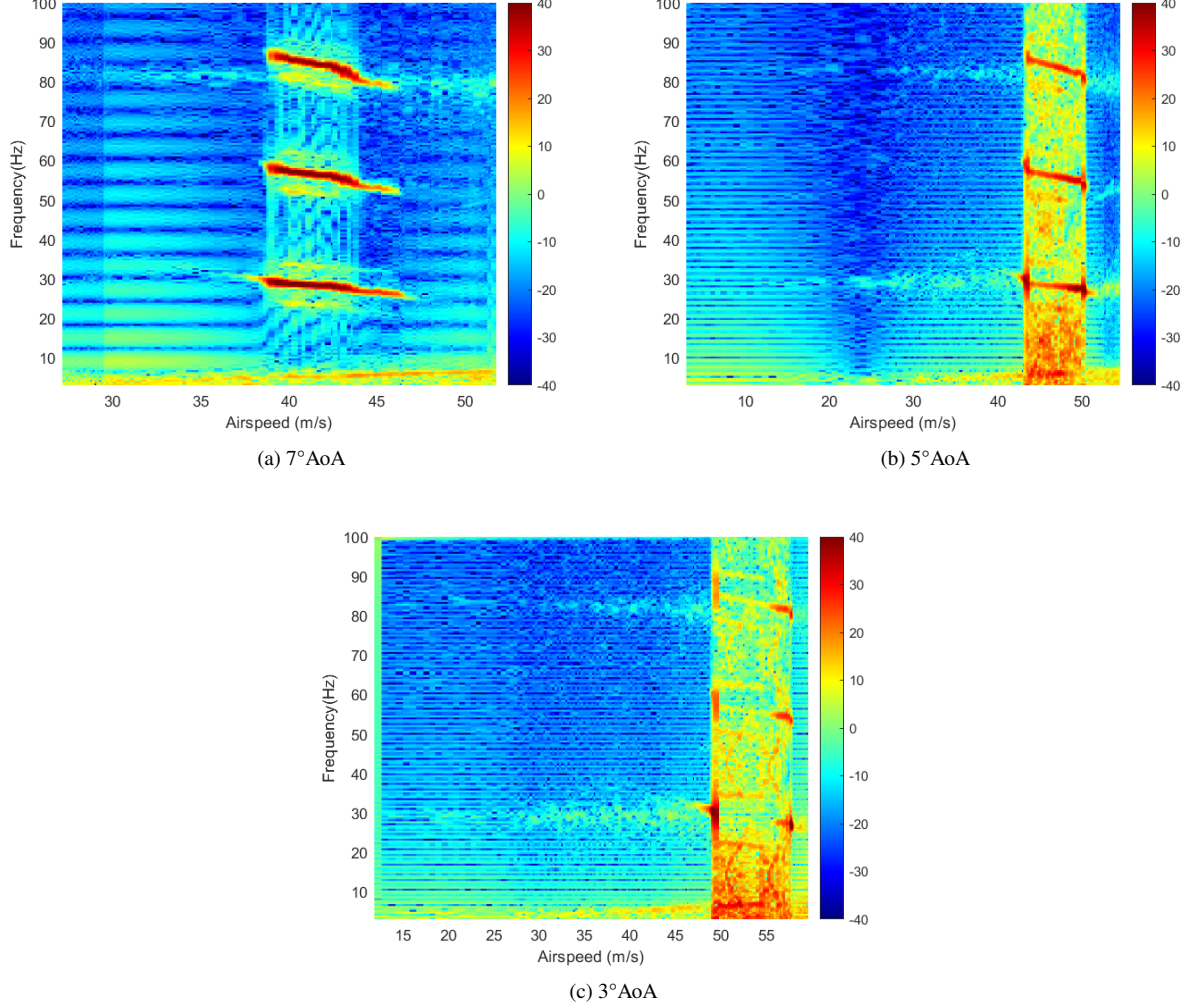


**Fig. 14 Oscillatory wingtip displacement and twist angle during flutter onsets at AoA of five degrees**

**Table 3 Flutter frequency and mode comparison**

AoA (°)	Frequency (Hz)	Twist to disp. amplitude ratio (°/ %span)	Twist to disp. phase (°)	Modal phase (°)
7 ↑	29.4	5.78	106	-74
5 ↑	29.9	5.16	113	-62
3 ↑	30.0	5.17	97	-83
5 ↓	26.7	3.95	152	-36
3 ↓	28.2	3.44	132	-48
2 – 2.5 ↓	27.2	3.1	130	50

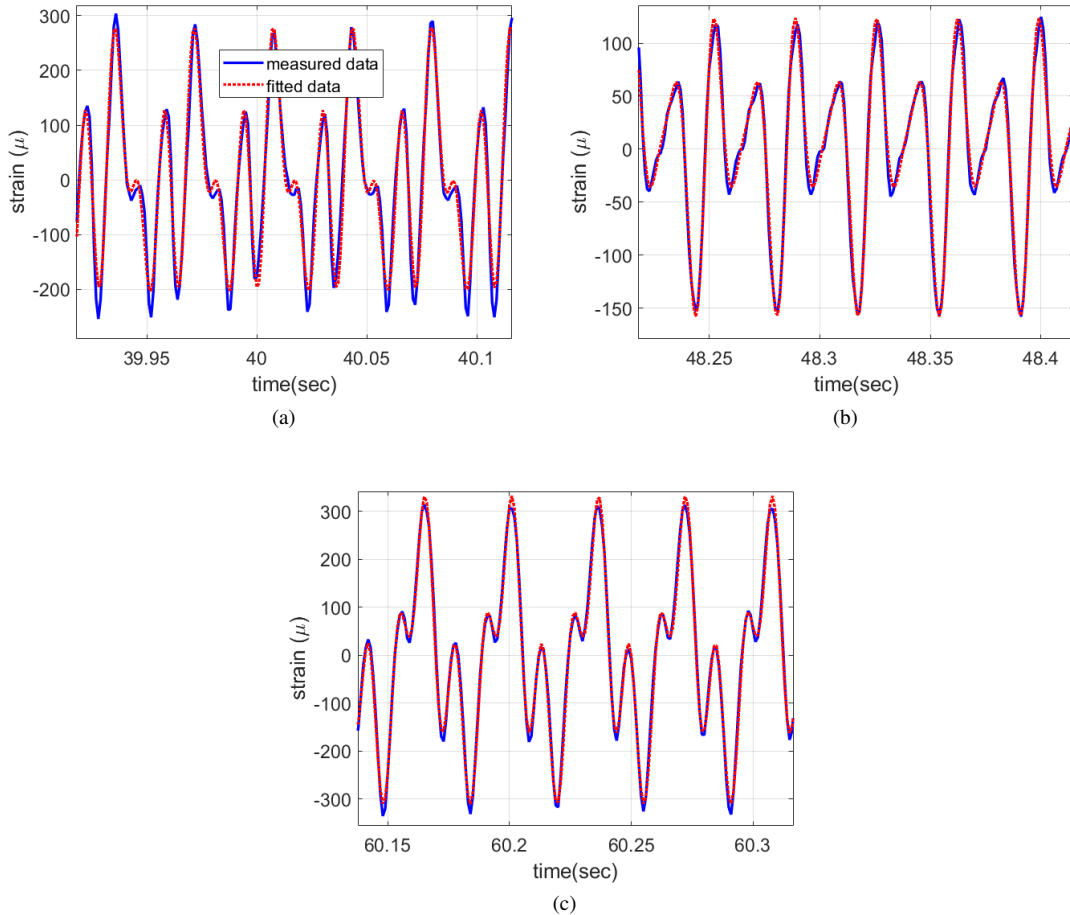
airspeed. The LCO regions are identified from the largely amplified first-torsion second-bending modal response, and a strong nonlinearity of the response is evident from the presence of the high harmonics.



**Fig. 15 Spectrograms of strain data from the three tests**

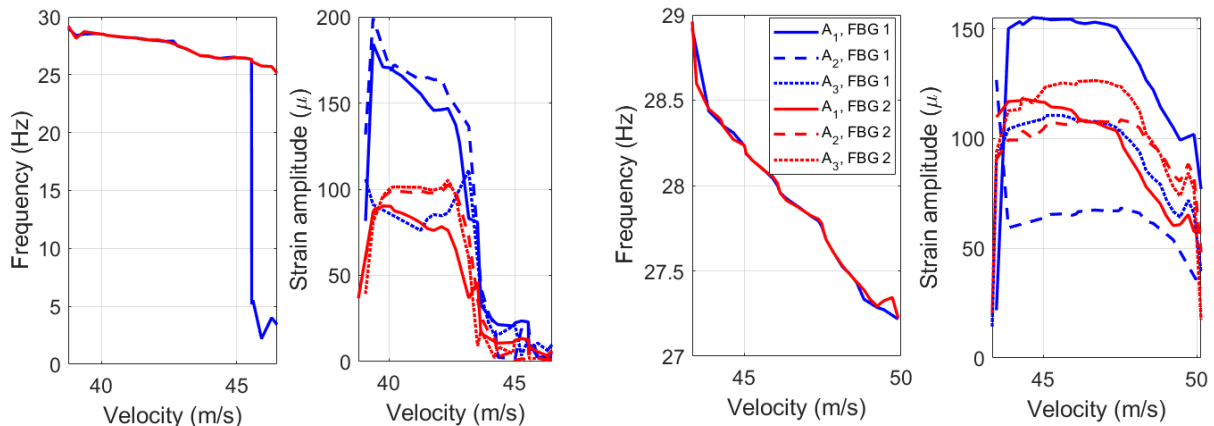
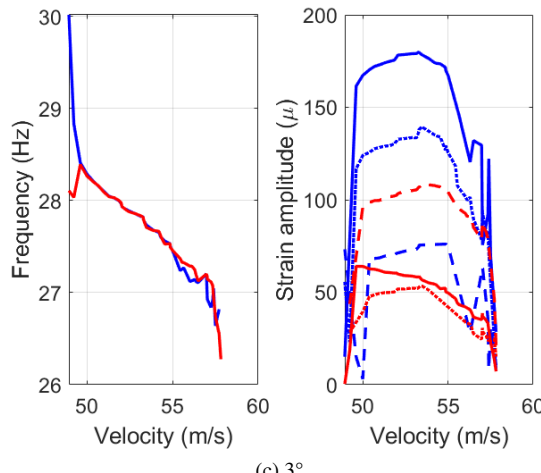
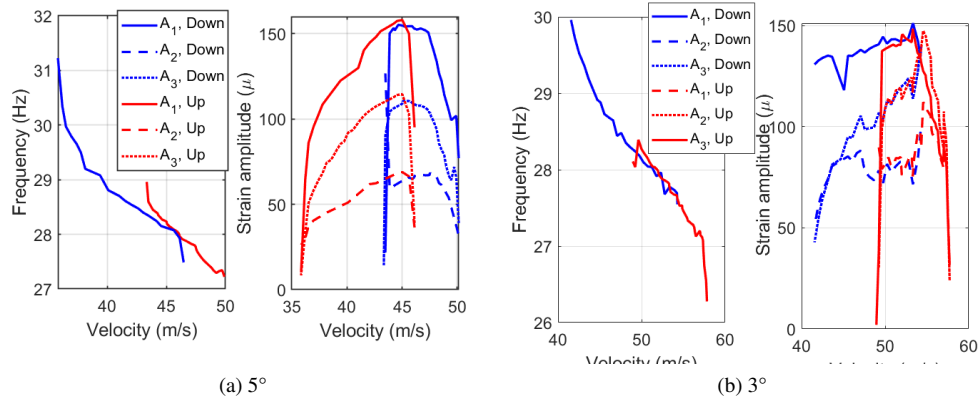
To further quantify the participation factor of the different harmonics, the oscillation time history was divided into subsections and each subsection was fitted with a sinusoidal function of the type:  $\varepsilon \approx \sum_{i=1}^3 A_i \sin(\omega_i t + \phi_i)$ . Sample strain time histories and their corresponding fitted data are presented in Fig. 16 for the test at AoA of seven degrees, showing that a three-term multi-sine function accurately describes the motion. In several cases, a fourth term is also present but its amplitude is small. Figure 17 shows the evolution of the frequencies and amplitudes of the sine terms during the up-sweeps. Only the frequency of the first harmonic is shown. However, the other two are exact multiples of the first (This is a result of the fitting and not a constraint). Results are shown for two arbitrary strain sensors in each of the three tests. The oscillation frequency reduces with the velocity. Additionally the significance of the higher harmonics is

evident as their amplitudes are of the same order of magnitude as the main frequency and even higher in some cases. It can also be seen that the dynamic response changes with velocity, not only in the amplitude but also in the ratio between the different harmonics.



**Fig. 16 Comparison of sample segments of the strain history to a fitted multi-sine function**

Figure 18 shows the results of the same sensor, at five and three degrees AoA, during the up and down sweeps. It is interesting to note that at LCO velocities (in velocities for which LCO exists in both the up and down sweeps), the LCO frequency and amplitude of all harmonics are similar and independent of the time histories.

(a)  $7^\circ$ (b)  $5^\circ$ (c)  $3^\circ$ **Fig. 17 Evolution of LCO with velocity at different tests**(a)  $5^\circ$ (b)  $3^\circ$ **Fig. 18 Comparison of LCO characteristics between up and down sweep tests**

## V. summary

The paper presented the flutter and LCO tests of the Pazy wing, a wind-tunnel benchmark of a very flexible wing. The test results are analyzed and compared with nonlinear aeroelastic analyses. Three velocity sweeps were performed at different angles of attack (AoA), during which the wing entered and exited LCO. A motion recovery camera system and fiber-optics Bragg grating sensors were used to track the deformations and strains over the wingspan. The wing encountered LCO when the wingtip deformation was approximately 25% of the span. The onset velocity, frequency, and mode shape varied depending on the test's AoA. An analysis of the flutter onsets showed large wingtip twist angles of over 10° in the flutter mode compared to deformation of only a few percent of the span, suggesting that the primary source of nonlinearity in the oscillating system is aerodynamic stall. The wing's LCO response was nonlinear, as evident by the significant frequency content of the high harmonics and its evolution with velocity increase. An increase in AoA led to a decrease in the flutter velocity and a slight reduction in the flutter frequency. Differences were observed between the LCO onsets during velocity up-sweep (i.e., when the wing entered LCO at a low velocity) and down-sweep (when the wing entered LCO at a high velocity). These differences were mainly in the frequency and twist-to-deflection ratio, which were lower at the down-sweeps, and the smaller phase angle between the displacement and twist modes. Significant hysteresis was observed in the system, leading to different flutter onset and offset velocities during velocity up and down sweeps, attributed to a supercritical type of bifurcation. Strain data analysis during the LCO showed that, given an LCO at a prescribe velocity, the frequency content was similar and independent of the initial conditions despite the hysteretic behavior. All the data and the Pazy wing models are publicly available through the 3rd Aeroelastic Prediction Workshop (<https://nescacademy.nasa.gov/workshops/AePW3/public>). Hopefully, this large dataset can serve in future studies validating computational models of very large deformations and studying various aspects of the aeroelastic response of flexible wings.

## Acknowledgement

The authors would like to gratefully acknowledge the support of the Pazy Foundation in this research project.

## References

- [1] Avin, O., Raveh, D. E., Drachinsky, A., Ben-Shmuel, Y., and Tur, M., “An Experimental Benchmark of a Very Flexible Wing,” *AIAA Scitech 2021 Forum*, 2021.
- [2] Goizueta, N., Drachinsky, A., Wynn, A., Raveh, D. E., and Palacios, R., “Flutter predictions for very flexible wing wind tunnel test,” *AIAA Scitech 2021 Forum*, 2021.
- [3] Drachinsky, A., and Raveh, D. E., “Aeroelastic Analysis of Very Flexible Wing Models Using the Modal Rotation Method,” *SciTech*, 2021.
- [4] Carre, A., Muñoz-Simón, A., Goizueta, N., and Palacios, R., “SHARPy : A dynamic aeroelastic simulation toolbox for very flexible aircraft and wind turbines,” *Journal of Open Source Software*, Vol. 4, No. 44, 2019, p. 1885. doi:10.21105/joss.01885.
- [5] ZAero *Theoretical Manual* V. 9.2, Scottsdale, AZ, 3<sup>rd</sup> ed., 2017.
- [6] Drachinsky, A., and Raveh, D. E., “Modal Rotations: A Modal-based Method for Large Structural Deformations,” *AIAA Journal*, Vol. 58, No. 7, 2020, pp. 3159–3173. doi:10.2514/1.J058899.
- [7] Drachinsky, A., Freydin, M., and Raveh, D. E., “Large Deformation Shape Sensing Using a Nonlinear Strain To Displacement Method,” *SciTech*, 2022.